AGU PUBLICATIONS

Water Resources Research

RESEARCH ARTICLE
10.1002/2017WR022159

Assessment of CO_2 Storage Potential in Naturally Fractured Reservoirs With Dual-Porosity Models

Rafael March[1], Florian Doster[1], and Sebastian Geiger[1]

[1]Institute of Petroleum Engineering, Heriot-Watt University, Edinburgh, UK

Key Points:
- We develop an estimate for brine drainage time scales by supercritical CO_2 during carbon storage in fractured formations
- We develop a new transfer function based on this time scale estimate that improves existing transfer functions for dual-porosity models
- We illustrate with simulations of injection scenarios into a fractured anticline that carbon storage in a naturally fractured reservoir is possible

Correspondence to:
F. Doster,
f.doster@hw.ac.uk

Citation:
March, R., Doster, F., & Geiger, S. (2018). Assessment of CO_2 storage potential in naturally fractured reservoirs with dual-porosity models. *Water Resources Research*, *54*, 1650–1668. https://doi.org/10.1002/2017WR022159

Received 31 OCT 2017
Accepted 19 FEB 2018
Accepted article online 23 FEB 2018
Corrected 28 MAR 2018 and 24 SEP 2018
Published online 8 MAR 2018

This article was corrected on 28 MAR 2018 and 24 SEP 2018. See the end of the full text for details.

Abstract Naturally Fractured Reservoirs (NFR's) have received little attention as potential CO_2 storage sites. Two main facts deter from storage projects in fractured reservoirs: (1) CO_2 tends to be nonwetting in target formations and capillary forces will keep CO_2 in the fractures, which typically have low pore volume; and (2) the high conductivity of the fractures may lead to increased spatial spreading of the CO_2 plume. Numerical simulations are a powerful tool to understand the physics behind brine-CO_2 flow in NFR's. Dual-porosity models are typically used to simulate multiphase flow in fractured formations. However, existing dual-porosity models are based on crude approximations of the matrix-fracture fluid transfer processes and often fail to capture the dynamics of fluid exchange accurately. Therefore, more accurate transfer functions are needed in order to evaluate the CO_2 transfer to the matrix. This work presents an assessment of CO_2 storage potential in NFR's using dual-porosity models. We investigate the impact of a system of fractures on storage in a saline aquifer, by analyzing the time scales of brine drainage by CO_2 in the matrix blocks and the maximum CO_2 that can be stored in the rock matrix. A new model to estimate drainage time scales is developed and used in a transfer function for dual-porosity simulations. We then analyze how injection rates should be limited in order to avoid early spill of CO_2 (lost control of the plume) on a conceptual anticline model. Numerical simulations on the anticline show that naturally fractured reservoirs may be used to store CO_2.

1. Introduction

There is a growing concern about the rising levels of anthropogenic CO_2 in the atmosphere, as they are one of the major contributors to the greenhouse effect. During the past two decades, the identification and development of reliable and effective techniques to mitigate the environmental effects of the greenhouse gases have been a focus of the scientific research community. These techniques include Carbon Capture and Utilization (CCU), Negative Emission Technology (NET), and Carbon Capture and Storage (CCS) (Cuellar-Franca & Azapagic, 2015; IPCC, 2005; Ringrose, 2017).

In particular, geological storage of CO_2 is regarded as an important technique to achieve the targets of temperature increase established in the last decade and updated during the Paris climate agreement negotiated in December 2015. Pacala and Socolow (2004) argued that a mix of different technologies, including CCS, will have to be employed in order to solve the climate problem for the next five decades. They estimated that 3,500 projects of the size of the *Sleipner* CCS project in the North Sea would be required to solve one-seventh of the global temperature increase problem. Celia et al. (2015) later updated these numbers, using present-day data, and calculated that this number of projects would solve just one-tenth of it. Therefore, the number of CCS projects needs to increase considerably to have a noticeable impact on the environment. At this scale, the availability of geological formations suitable for CO_2 injection at locations that allow economic operations is a limiting factor that hinders the global implementation of carbon storage.

Fractured reservoirs are ubiquitous in sedimentary basins across the world. Estimates suggest that more than half of the world's remaining conventional hydrocarbon resources are stored in extensively fractured carbonate reservoirs (Burchette, 2012). However, these reservoirs have received little attention as potential candidates for CO_2 storage. Yet, they offer a significant potential for combining CO_2 storage with enhanced oil recovery (Agada et al., 2016). The primary reason seems to be related to the fact that for most formations, CO_2 is the nonwetting phase relative to the resident fluid. Since capillary pressure in the fractures is typically orders of magnitude lower than in the rock matrix, capillary forces may prevent CO_2 from invading

the rock matrix. This could severely impact the storage potential of the aquifer, as the matrix generally accounts for most of the pore volume. This negative effect may be specially evident in aquifers with small thickness (<50 m) or with a set of near-horizontal fractures with apertures that are large enough to prevent the creation of capillary bridges across the vertical section. Fractures also have high conductivity and the presence of an interconnected system of fractures may lead to fast flow of CO_2 through the fracture system, without significant storage in the rock matrix. This could lead to a loss in control of the CO_2 plume, and potentially to CO_2 leakage through abandoned wells or reactivated faults. Despite these challenges, the study of CO_2 storage in fractured formations is very relevant to the global implementation of CCS. Since fractures are a major source of uncertainty in geological formations, the existence of a previously unidentified fracture system should be incorporated in the risk analysis of storage projects. Moreover, as fractured reservoirs are numerous, they may be considered as storage site as the number of CCS projects increases. The ability to model and simulate the multiphase dynamics in such formations is of utmost importance to the development of a storage project.

Techniques to simulate flow in fractured porous rocks are typically separated in two large families of methods. The first family includes methodologies that explicitly represent the fractures as geometrical features in the simulation model. Pertaining to this family are the Discrete Fracture and Matrix (DFM) methods (e.g., Geiger et al., 2009; Karimi-Fard et al., 2004; Moinfar et al., 2013; Schmid et al., 2013), and the Embedded Discrete Fracture Model (EDFM) (e.g., Fumagalli et al., 2016; Moinfar et al., 2014; Shah et al., 2016). One limitation of this family of methods is that they do not generally allow the representation of all fractures at the reservoir scale due to computational complexities. The second family includes methods that consider the fractures as a second continuum. Of particular importance in such class of methods are the Dual Porosity (Kazemi et al., 1976; Warren & Root, 1963), the Dual-Porosity Dual-Permeability (Kazemi et al., 1976), together with their extensions like the Multiple Interacting Continua (Pruess, 1985) and the Multi-Rate Dual-Porosity methods (Di Donato et al., 2007; Geiger et al., 2013; Maier & Geiger, 2013; Tecklenburg et al., 2016). Multiple-continuum methods are popular in the reservoir simulation community due to their computational efficiency, as they are based on the upscaling of the fracture system properties instead of representing each individual fracture. A key element of these upscaled methods are mass transfer functions that model the fluid exchange between fractures and matrix. The modeling of multiphase fluid transfer between both continua is a challenging task that has been addressed extensively, but is not fully solved; we refer to Lemonnier and Bourbiaux (2010a), Abushaikha and Gosselin (2008), Al-Kobaisi et al. (2009), and Ramirez et al. (2009) for comprehensive reviews. While the understanding of multiphase dynamics in porous media has been advanced throughout the years, the first transfer functions developed by Kazemi et al. (1976) remain popular due to their simplicity and ability to address different physical mechanisms. Several modifications of these functions were suggested (e.g., Al-Kobaisi et al., 2009). However, none of them focus on CO_2-brine systems. The development of a transfer function that captures the drainage of brine by supercritical CO_2 requires an estimate of the time scale of the drainage process.

In this manuscript, we hence develop an estimate of the order of magnitude of the time scale of CO_2-induced matrix-block drainage, by extending the work of Di Donato et al. (2006). This time scale consists of a model to estimate the time it takes to saturate a matrix block to equilibrium, and hence is an important component to understand the dynamics of CO_2 storage in NFRs. Moreover, it leads to a transfer function that accurately models gravity-drainage processes in the context of CO_2 storage. The application of this transfer function in the dual-porosity framework allows us to have a conceptual understanding of the impact of fractures during CO_2 storage operations.

This paper is structured as follows: in section 2, we provide a general overview of the dynamics of CO_2 in naturally fractured reservoirs and present the governing equations as well as simplifying assumptions for single-porosity and dual-porosity porous media. Section 3 comprises the main part of this work. It presents an analysis of storage capacity and drainage time scales for a single matrix block via numerical simulation of fully resolved matrix blocks. It then provides a novel model to estimate the time scale of matrix-block drainage and a new transfer function based on this time scale estimate. This model enables CCS simulations with dual-porosity models. Finally, at the end of this section, the performance of this transfer function is compared with the ones given by other transfer functions that are popular in commercial and open-source simulators. In section 4, we consider a conceptual anticline geometry to evaluate the impact of fractures on field-scale storage using dual-porosity simulations. We also suggest a model that is based on the time scale

estimate developed in section 3 and that limits the injection rate to avoid the early spill of CO_2. Finally, in section 5, we provide a summary of the main results and contributions of this work, together with some general guidelines regarding CO_2 storage operations in NFRs.

2. CO_2 Storage Dynamics in NFR's

We start the discussion by reviewing the main physical mechanisms that take place during CO_2 injection in fractured formations. We focus our discussion on fractured saline aquifers, because saline aquifers have the largest storage potential (IPCC, 2005). CO_2 storage operations target geological formations whose temperature and pressure conditions are such that CO_2 is in supercritical state. In this state, the gas density increases significantly, which improves its stored mass per unit pore volume. Typical values for CO_2 density range from 266 to 733 kg/m^3, depending on the pressure and temperature conditions of the formation. The compressibility, on the other hand, ranges typically from 10^{-9} to 10^{-8} Pa^{-1}, which is at least one order of magnitude lower than that of a gas (Law & Bachu, 1996). Brine density is more sensitive to the salinity of the water, with values ranging from 945 to 1,230 kg/m^3 (Nordbotten & Celia, 2012); its compressibility is of the order of 10^{-10} Pa^{-1}. The density of brine is therefore always larger than the density of CO_2, and this density difference induces upward flow of CO_2. Therefore, suitable geological formations for storage should be overlaid by a capping formation that prevents CO_2 from rising to the surface. CO_2 will also dissolve in the resident brine, with typical values of solubility by mass ranging from 1% to 6% (Spycher et al., 2003). The dissolution of CO_2 leads to an increase in the density of brine, which may create an unstable system and therefore the generation of convective dissolution cells. The convective dissolution of CO_2 in brine has been identified as an important mechanism for safe storage of CO_2 in unfractured saline aquifers (Emami-Meybodi & Hassanzadeh, 2015; Macminn et al., 2011; Riaz et al., 2006; Suekane et al., 2008). Therefore, the injection of CO_2 in a saline aquifer gives rise to a multiphase multicomponent system, with distinct time scales associated with buoyancy, injection, and mass transfer between the phases.

Modeling of fractured formations is a challenging task as the fractures introduce additional time scales to the system. An interconnected system of fractures can act as a high-permeability pathway that enables rapid fluid flow. Hence, injected CO_2 can quickly travel through the fracture system, while its transfer to the rock matrix will occur at an usually slower time scale (Figure 1a). Fracture-matrix transfer mechanisms were extensively studied through laboratory and numerical experiments (e.g., Ahmed Elfeel et al., 2016; Fernø et al., 2013; Lemonnier & Bourbiaux, 2010b; Lu et al., 2008). Figure 1b summarizes the most relevant transfer mechanisms. If the permeabilities of fracture and matrix are comparable or if there is capillary continuity between the matrix blocks, CO_2 may enter the rock matrix blocks by viscous displacement. Otherwise, fractures will quickly transport the CO_2 phase, creating isolated systems of brine-saturated matrix blocks

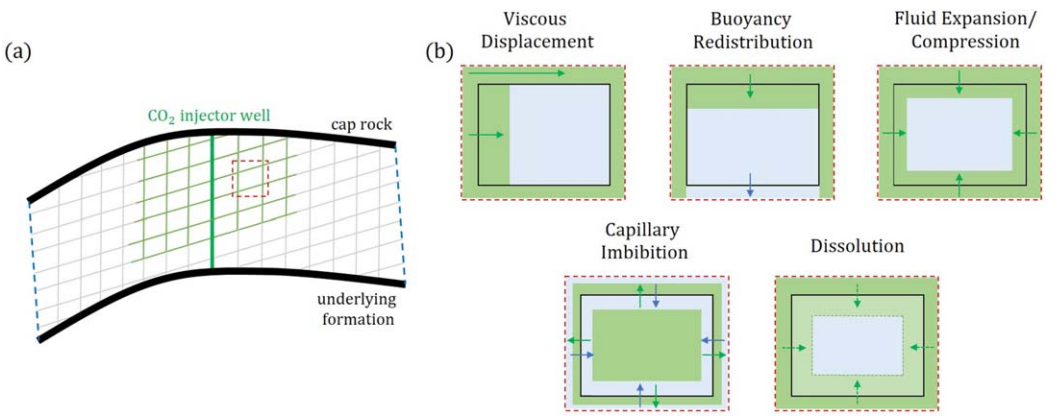

Figure 1. (a) Conceptual representation of CO_2 injection in a fractured reservoir. Injected CO_2 (in green color) quickly saturates the fractures (light-gray lines), that generally have low pore volume and high permeability. (b) Conceptualization of different transfer mechanisms responsible for transfer of CO_2 (green) and brine (blue) between a matrix block and the surrounding fractures. Geomechanical effects in the transfer are neglected here, but may be important for some formations. Arrows indicate the main direction of CO_2 and brine flow on each mechanism (green and blue, respectively). The dominant mechanisms in a well-connected fracture network are buoyancy redistribution and capillary imbibition.

surrounded by CO_2 saturated fractures. Each matrix block is not in equilibrium in this configuration, as brine is heavier than CO_2 and will redistribute with the supercritical fluid, during a drainage process caused by the contrast between capillary and gravity forces (mechanism named "buoyancy redistribution" in Figure 1b). When the injection rate is reduced or injection stops, fractures otherwise saturated by CO_2 may be filled by water. Capillary forces then cause the wetting phase to imbibe the rock matrix, displacing CO_2 back to the fractures (March et al., 2016) (mechanism named "capillary imbibition" in Figure 1b). This process may lead to trapping of CO_2 phase in the pores of the rock due to the hysteretic nature of the relative permeability (Juanes et al., 2006).

We believe these two mechanisms—gravity drainage during CO_2 injection phase followed by capillary imbibition during plume migration when injection stops—are the main mechanisms responsible for fluid transfer between fractures and matrix during CO_2 storage operations in NFRs. Other mechanisms like viscous transfer, fluid compression, and dissolution are unlikely to contribute to the transfer of CO_2 to the matrix during the injection phase. Viscous transfer may be relevant in the near-well region, where large pressure gradients induced by the well may generate a horizontal component inside the matrix blocks. However, since we consider NFRs with an interconnected system of fractures and good permeability contrast between fracture and matrix, far from the near-well region pressure gradients experienced by the formation will generally lead to a fast flow of CO_2 in the fractures, with a negligible amount of CO_2 invading the matrix due to viscous displacement. CO_2 dissolution in brine happens at time scales of hundreds of years, much slower than the typical time scales of CO_2 injection considered here. Convection-driven dissolution ("density fingers") is regarded as a key physical mechanism to shorten this time scale (Riaz et al., 2006). The high-permeability fractures, however, represent a preferential pathway for the development of convection cells. This hinders the development of convection cells within the matrix blocks. Finally, the fact that the brine that is initially resident in the matrix blocks has very low compressibility allows us to neglect the transfer due to brine compression during CO_2 injection. A quick and conservative estimate allows us to estimate the time scale of pressure equilibration inside a matrix block. Considering a permeability of $k_m = 1$ mD, a porosity of $\phi_m = 0.1$, a brine compressibility of $c = 10^{-10}$ Pa^{-1}, a viscosity of $\mu_w = 1$ cP and a characteristic block dimension of $L = 100$ m, the pressure diffusion time scale is estimated by $T \approx L^2/\eta$, with $\eta = k_m/\phi_m \mu_w c$. This yields an equilibration time of ≈ 1 day. The equilibration time can be considered instantaneous when compared to the operation's time scale, which is in the order of years.

An ideal CO_2 operation in an NFR maximizes the amount of CO_2 in the rock matrix. In other words, it is undesirable that CO_2 remains in the fractures, as the CO_2 plume may quickly flow through the fractures and reach a leakage pathway through the cap rock or an abandoned well. Therefore, the development of a model that describes the time scale of CO_2 transfer due to gravity drainage (commonly denoted a transfer function in the dual-porosity modeling framework) is important to design efficient storage operations. In the next subsections, we analyze the time scales and stored amount of CO_2 in a matrix block from numerical simulations and develop a time scale estimate for brine drainage by supercritical CO_2.

2.1. Governing Equations

We now introduce the system of conservation equations for the wetting (brine) and nonwetting phases (CO_2), that together with the multiphase extension for Darcy's law and appropriate boundary conditions form a closed set of partial differential equations that describe the flow of compressible immiscible fluids in porous media (Bear, 1972):

$$\begin{aligned} &\frac{\partial(\phi \rho_\alpha S_\alpha)}{\partial t} + \nabla \cdot (\rho_\alpha \mathbf{q}_\alpha) = \tilde{q}_\alpha, \\ &\mathbf{q}_\alpha = -\mathbf{k} \lambda_\alpha (\nabla p_\alpha - \rho_\alpha \mathbf{g}), \end{aligned} \tag{1}$$

where S_α is the saturation of phase α, ρ_α its density, $\tilde{q}_\alpha$ mass source terms (e.g., due to wells), and ϕ and $\mathbf{k}$ the porosity and permeability of the porous medium. The multiphase Darcy model relates the Darcy velocity $\mathbf{q}_\alpha$ of phase α with the gradient of the phase's pressure p_α and its mobility, defined as $\lambda_\alpha = k_{r\alpha}/\mu_\alpha$, where μ_α is its viscosity and $k_{r\alpha}$ is the relative permeability to phase α. Phase pressures are related by the capillary pressure through the expression $p_n = p_w + p_c(S_w)$. For simplicity, in the remainder of this text, we assume Corey-type relationships for the relative permeability and capillary pressure. Therefore, we write $k_{r\alpha} = k_{r\alpha}^{\max} S_{\alpha e}^{n_\alpha}$ and $p_c(S_w) = P_e S_{we}^{-n_p}$, where $S_{\alpha e}$ is the effective saturation, normalized by the residual saturations, and n_α

and n_p are the power law exponents of the relative permeabilities and capillary pressure. We disregard geomechanical effects here, noting that the main mechanical effects of CO_2 injection in fractures (increased fracture transmissivity due to fracture opening) and matrix (potential block shrinkage due to rock compression, leading to brine transfer to matrix) are unlikely to change significantly the results shown in this work.

For incompressible fluids and solids, the conservation equations defined in equation (1) are identically represented by a single equation for the saturation of the wetting phase and an equation for the total flux $\mathbf{q}_t \equiv \mathbf{q}_w + \mathbf{q}_n$:

$$\begin{aligned} \nabla \cdot \mathbf{q}_t &= \tilde{q}_w/\rho_w + \tilde{q}_n/\rho_n, \\ \phi \frac{\partial S_w}{\partial t} + \nabla \cdot \mathbf{q}_w &= \tilde{q}_w/\rho_w, \\ \mathbf{q}_w &= f_w \mathbf{q}_t + k f_w \lambda_n \frac{dp_c}{dS_b} \nabla S_b + (\rho_w - \rho_n) g \nabla z, \end{aligned} \tag{2}$$

where $f_\alpha = \lambda_\alpha/\lambda_t$, and $\lambda_t = \lambda_w + \lambda_n$ is the fractional flow of phase α. In this work, CO_2 and brine are assumed to be incompressible due to the low compressibility of brine and CO_2 in supercritical state. The average densities of the fluids are defined by the depth and temperature conditions of the target storage formation.

2.2. Dual-Porosity Formulation

The direct utilization of equations (1) or (2) to simulate the flow in NFR's is prohibitively expensive for most of the realistic geological models; this would require the explicit representation of each fracture by either conforming the simulation grid to them (e.g., Karimi-Fard et al., 2004) or by embedding them in the computational mesh (e.g., Fumagalli et al., 2016). Dual-continuum approaches (Kazemi et al., 1976; Warren & Root, 1963), on the other hand, have been widely used in the past decades since they do not require explicit fracture representation in the computational model. Instead, the fracture system is represented as a second continuum that is superposed to the rock matrix. The two continua are related by an upscaled transfer term T that models the mass transfer between the two continua. Equations (1) are extended by a set of conservation equations for the rock matrix. We then write:

$$\begin{aligned} \frac{\partial(\phi_f \rho_{wf} S_{wf})}{\partial t} + \nabla \cdot (\rho_{wf} \mathbf{q}_{wf}) &= \tilde{q}_w - T_w, \\ \frac{\partial(\phi_f \rho_{nf} S_{nf})}{\partial t} + \nabla \cdot (\rho_{nf} \mathbf{q}_{nf}) &= \tilde{q}_n - T_n, \\ \frac{\partial(\phi_m \rho_{wm} S_{wm})}{\partial t} &= T_w, \\ \frac{\partial(\phi_m \rho_{nm} S_{nm})}{\partial t} &= T_n, \end{aligned} \tag{3}$$

where the subscripts $\{f, m\}$ identify variables of the fracture and matrix continuum. The transfer rate term T_α models the rate of mass exchange of phase α between fracture and matrix per unit bulk volume. The transfer rate is a key ingredient of dual-porosity models, and although several expressions for this term exist in the literature, the development of a model that accurately capture the transfer mechanisms shown in Figure 1 is challenging and still an open topic of research. In particular, as shown in the next sections, current formulations of transfer functions fail to predict the drainage dynamics accurately. Therefore, the utilization of the dual-porosity model to evaluate CO_2 storage in NFRs requires a new model to capture gravity drainage.

We consider the dual-porosity model defined by equations (3) in this work to evaluate geological storage of CO_2 in NFRs. Dual-porosity models are applicable to naturally fractured reservoirs with a well-connected system of fractures and high-permeability contrast between both media (Bourbiaux et al., 2002). We limit our analysis to such reservoirs. One of the key contributions of this work is the development of an estimate for the time scale of CO_2 transfer from the fractures to the matrix blocks. This time scale provides an expression for the transfer terms T_α that captures the drainage of brine by CO_2 on a block scale with reasonable accuracy.

Table 1
Physical Parameters Used to Evaluate Gravity Drainage on a Block Scale

	Case	Values
Environment	Shallow-cold	ρ_w=1,012 kg/m^3, ρ_n=714 kg/m^3, μ_w=0.8 cP, μ_n=0.05 cP
	Shallow-warm	ρ_w=998 kg/m^3, ρ_n=714 kg/m^3, μ_w=0.8 cP, μ_n=0.05 cP
	Deep-cold	ρ_w=995 kg/m^3, ρ_n=733 kg/m^3, μ_w=0.38 cP, μ_n=0.06 cP
	Deep-warm	ρ_w=945 kg/m^3, ρ_n=479 kg/m^3, μ_w=0.2 cP, μ_n=0.04 cP
Sample	cardium#2 (Sandstone)	k = 21 mD, S_{wr} = 0.42, n_w=1.2, n_n=1.3, k_{rn}^{max}=0.13, ϕ_m=0.16
	viking#2 (Sandstone)	k = 21 mD, S_{wr} = 0.42, n_w=1.7, n_n=2.8, k_{rn}^{max}=0.26, ϕ_m=0.19
	Wabamun#2 (Sandstone)	k = 67 mD, S_{wr} = 0.57, n_w=1.4, n_n=2.1, k_{rn}^{max}=0.19, ϕ_m=0.15
	nisku#1 (Carbonate)	k = 46 mD, S_{wr} = 0.33, n_w=2.8, n_n=1.1, k_{rn}^{max}=0.18, ϕ_m=0.1
	cooking-lake (Carbonate)	k = 65 mD, S_{wr} = 0.48, n_w=1.4, n_n=5.6, k_{rn}^{max}=0.07, ϕ_m=0.1
Capillary Pressure Level	High-P_c	P_e = 40 kPa (match stick) and P_e = 25 kPa (sugar cube)
	Low-P_c	P_e = 10 kPa (match stick) and P_e = 5 kPa (sugar cube)

Note. Each combination of environment, sample, and capillary pressure level is considering, giving a total of 40 simulation cases. Environments follow the definition of Nordbotten and Celia (2012). Samples were extracted from experiments carried by Bennion and Bachu (2006). Two capillary pressure cases were considering respecting the maximum capillary entry pressure for CO_2 invasion, given the block size (L_z = 20 m).

3. Capacity and Drainage Time Scales for a Single Matrix Block

In section 2, we discussed that the fast flow of CO_2 in the fractures creates isolated systems of brine-saturated blocks. These blocks are drained by CO_2 if buoyancy is large enough to overcome the capillary entry pressure. There are two important aspects to be analyzed in this transfer process. The first is the maximum amount of CO_2 that can be stored in a matrix block that is surrounded by fractures saturated by CO_2. The maximum CO_2 volume gives a measure of the negative impact of fractures on CO_2 storage. The second is the time it takes for a matrix block that is being drained to reach equilibrium with the CO_2-saturated fractures. The drainage time provides a time scale for the CO_2 transfer to the matrix, and is important since a slow transfer process means that the CO_2 plume spreads farther in the fracture system and the potential for leakage is increased. In this section, we analyze the results of fully resolved numerical simulations of CO_2-brine drainage on three-dimensional matrix blocks.

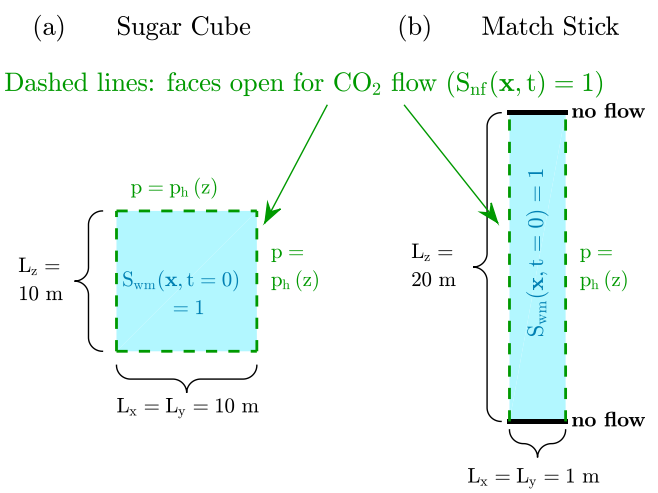

Figure 2. Conceptual picture of the block geometries and boundary conditions for (a) the sugar cube geometry and (b) the match stick geometry. Fractures are modeled as boundary conditions on the matrix blocks. Green dashed lines represent open boundary faces, open for CO_2 flow, while solid black lines in the match stick model represent no-flow boundaries. Only a projection in the *x-z* plane is shown, but geometries are 3-D with $L_y = L_x$.

3.1. Setup for a Single Matrix Block

In order to understand the dynamics of drainage at the scale of a matrix block, a series of simulations were run using MRST (Lie et al., 2011) to evaluate the amount of CO_2 stored in a block and the drainage time scale on a diverse number of CO_2 storage environments. A summary of the rock and fluid properties considered is provided in Table 1. As the drainage dynamics depend on the dimensions and aspect ratio of the matrix blocks, we consider two representative block geometries: a cubic block (L_x=L_y=L_z=10 m) and a tall block, with the vertical length much larger than the horizontal dimensions (L_x=L_y=1 m and L_z = 20 m) (see Figure 2). The cubic block represents a matrix block in a reservoir that has three perpendicular sets of fractures with sufficient aperture to prevent the formation of capillary bridges. Labastie (1990) has measured in experiments that—for a surface tension of 24 mN/m—apertures greater than 0.3 mm do not allow for the creation of capillary bridges. Therefore, the cubic block has all its faces open for flow, representing the typical "sugar cube" geometry (Warren & Root, 1963). The tall block has only the lateral faces open for flow (no-flow boundary conditions at top and bottom faces), representing a reservoir with no horizontal fractures, or with strong capillary continuity across the vertical blocks (sometimes referred to as "match stick" geometries). Blocks with similar aspect ratio are seen in fractured outcrops (Egya et al., 2018) and in the In

Salah CO_2 storage project (Eiken et al., 2011; Iding & Ringrose, 2010). Note, that we do not consider cases where the horizontal fracture spacing is much larger than the reservoir thickness. Fractures are modeled as boundary conditions on the matrix blocks. Fractures usually have very high permeability, and therefore injected CO_2 should quickly segregate in the fracture system and reach hydrostatic equilibrium (Guo et al., 2014). Hence, in both models, the open faces are prescribed with hydrostatic CO_2 pressure. The model was discretized with uniform grid cells of $\Delta x=\Delta y=\Delta z=10$ cm. A constant time step of $\Delta t=0.1$ day was considered for all simulations. This discretization was shown to be sufficient to capture the dynamics for all the simulation cases.

To cover representative scenarios for CO_2 storage, we consider four different storage environments, representing formations at shallow and deep depths in warm or cold basins (Nordbotten & Celia, 2012). These cases are named shallow-cold, deep-cold, shallow-warm, and deep-warm. "Shallow" formations are located at 1 km depth, while "deep" formations at 3 km depth. "Cold" basins have a surface temperature of 10°C and geothermal gradient of 25°C/km, while "warm" basins have a surface temperature of 20°C and geothermal gradient of 45°C/km. We consider low-salinity brines. The corresponding densities and viscosities of the fluids for each of the four environments, from Nordbotten and Celia (2012), are given in Table 1. Representative values for porosity, residual brine saturation, absolute and relative permeability parameters are taken from five samples (two sandstones and three carbonates) from Bennion and Bachu (2008). We keep their sample names and refer to them as viking#2, cardium#2, wabamun#2, nisku#1, and cooking-lake. The parameters are given in Table 1. Since there is no capillary pressure data available for the five selected samples, we consider two capillary pressure levels, a "low-P_c" and a "high-P_c" case (see Table 1). Capillary pressure depends on a series of parameters that are generally uncertain and difficult to measure in situ, such as surface tension and contact angle between the phases, and therefore we have decided to change this parameter to cover these two possible scenarios. In the remainder of this text, each simulation case will be labeled as {sample}-{environment}-{pc level} (e.g., cardium#2-deep-cold-low-P_c). A total of 2 shapes $\times$ 4 environments $\times$ 5 samples $\times$ 2 P_c levels = 80 simulations were considered in this analysis.

3.2. Capacity and Drainage Time Scales From Numerical Simulations

In this section, we discuss the results of the numerical simulations by analyzing the maximum volume of CO_2 that invaded the block when the fluids reach an equilibrium, denoted as $V_{CO_2}^{max}$, the maximum mass of CO_2 in the block at this point, denoted as $M_{CO_2}^{max}$, and the time it takes to reach equilibrium, denoted as t_{95}. We take t_{95} from the numerical simulations as the time when the volume of CO_2 inside the block corresponds to 95% of $V_{CO_2}^{max}$. As the lateral faces are open for flow and at hydrostatic pressure of CO_2, in equilibrium the phase pressures are hydrostatic and their difference is compensated by capillary pressure. The final saturation profile is calculated analytically by evaluating the inverse of the capillary pressure at the difference between hydrostatic pressures for each depth: $S_n^{\infty}(z)=1-p_c^{-1}(\Delta\rho g(L_z-z))$, where $\Delta\rho=\rho_w-\rho_n$ and the z axis denotes depth. This gives a maximum volume of $V_{CO_2}^{max}=\phi_m L_x L_y \int_{z=0}^{z=L_z} S_n^{\infty}(z)dz$. The maximum volume is calculated analytically based on the rock and fluid properties for each simulation case. The maximum mass is calculated by multiplying the maximum volume by the density of CO_2, $M_{CO_2}^{max}=\rho_{CO_2}V_{CO_2}^{max}$. We also define the pore volume that is effectively used for storage, $V_{CO_2}^{\%}=V_{CO_2}^{max}/(\phi_m(1-S_{wr})V_b)$, where V_b is the volume of the block. This parameter allows us to evaluate the storage loss due to the presence of fractures.

Figure 3 shows the results of the numerical simulations for the sugar cube block. We restrict the analysis in this section to this block shape, noting that it also applies for the match stick geometry. The circles are inversely scaled according to the capillary pressure level (small circles correspond to high-P_c and large circles correspond to low-P_c). The circle fill colors correspond to different environments (shown in the legend of the picture), while the color of the edges correspond to different samples (shown in the picture).

The drainage time, t_{95}, shows a large variation across the different cases, ranging from $t\approx 10$ days to $t\approx 355$ days. It is therefore an important metric to be observed during storage operations. In the low-P_c cases, the largest drainage times are seen in the viking#2 and nisku#1 samples, due to their larger effective pore volume and lower permeability. The shallow-cold environment leads to higher times compared to the deep-cold, which is more evident for the nisku#1 sample ($t\approx 355$ days versus $t\approx 150$ days). This is due to the larger viscosity ratio between CO_2 and brine in deep-cold compared to shallow-cold environments ($\mu_n/\mu_w\approx 0.157$ versus $\mu_n/\mu_w\approx 0.06$). The deep-warm environment shows the largest value of viscosity ratio, which explains why the yellow circles are concentrated on the left half of the plot ($\mu_n/\mu_w\approx 0.2$). The

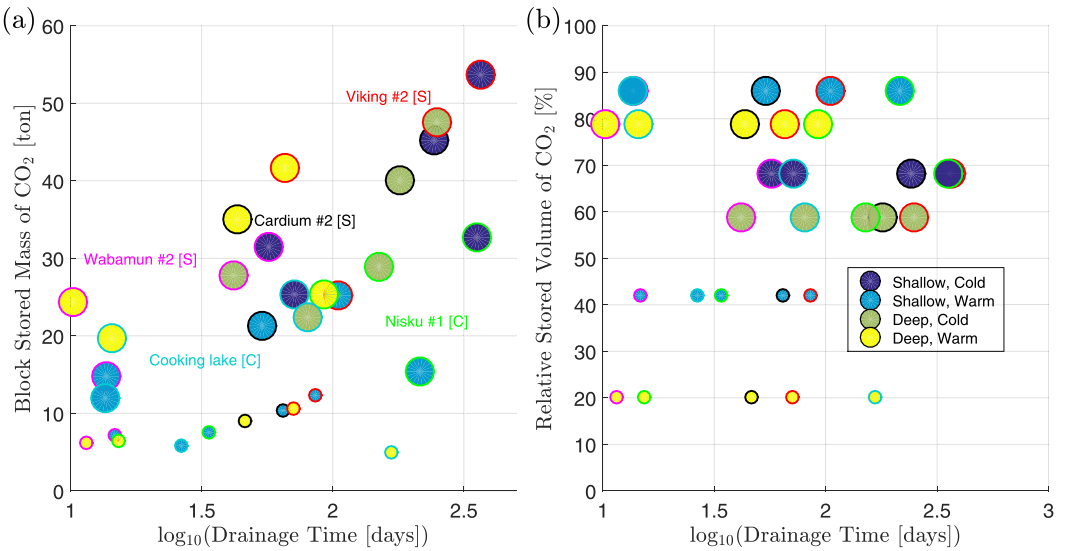

Figure 3. Analysis of the maximum CO_2 storage and drainage time scales on a single block for the sugar cube geometry. (a) Drainage time versus stored mass of CO_2; (b) Drainage time versus relative stored volume of CO_2. The relative volume provides a percentage measure of the pore volume not effectively used for storage due to the presence of a fracture system. Small circles correspond to high-P_c cases.

wabamum#2 sample has similar properties to that of the cooking-lake. Hence, they show similar maximum masses and drainage times for each environment in the low-P_c cases. However, a high contrast in t_{95} is seen between these samples for the deep-warm, high-P_c cases ($t_{95} \approx 11$ days versus $t_{95} \approx 133$ days). The unfavorable conditions seen in the cooking-lake sample are due to very high Corey exponent for the CO_2 relative permeability ($n_n = 5.6$), that slows down drainage. This effect is less evident when buoyancy forces are very strong. In fact, in hydrocarbon recovery operations, the assumption of $\mu_w \gg \mu_n$ usually leads to an equation for the nonwetting phase invasion that completely disregards the influence of the nonwetting phase (Hagoort, 1980). That is, if buoyancy is high enough and the viscosity of the wetting phase is much larger than the viscosity of the nonwetting phase, the wetting phase dominates the flow and the nonwetting phase only occupies the void space without creating any resistance to flow. However, this is not always the case in CO_2 storage operations. In supercritical state, CO_2 has its viscosity increased, decreasing the viscosity contrast between CO_2 and brine. This is reflected in the high drainage times seen in the cooking-lake-high-P_c case due to high n_n.

While $M^{\max}_{CO_2}$ changes for each sample due to different porosities and S_{wr}, $V^{\%}_{CO_2}$ changes only with the environment and the capillary pressure level, as this parameter is normalized by the effective pore volume for each case. One of the key parameters to understand the behavior of the block stored mass and volume is the density difference between brine and CO_2. It determines the maximum penetration depth of the CO_2 front. The shallow-warm environment has a higher $\Delta\rho$ ($\Delta\rho = 732$ kg/m^3), while the deep-cold has a lower $\Delta\rho$ ($\Delta\rho = 222$ kg/m^3). Therefore, the shallow-cold and deep-cold environments show different values for the CO_2 storage volume: $V^{\%}_{CO_2} \approx 85\%$ and $V^{\%}_{CO_2} \approx 60\%$, respectively, for the low-P_c case (Figure 3b). On the other hand, cold basins lead to the highest values of CO_2 density, as ρ_{CO_2} increases with decreasing temperature ($\rho_n = 714$ kg/m^3 and $\rho_n = 733$ kg/m^3 for shallow-cold and deep-cold environments). Hence, more CO_2 is stored. This explains the behavior of the shallow-cold and deep-cold environments in the upper part of Figure 3a. In short, high ρ_{CO_2} implies low $\Delta\rho$ and therefore low $V^{\%}_{CO_2}$, but also implies high $M^{\max}_{CO_2}$. This is an interesting competing behavior of the CO_2 density that is only seen in fractured formations.

In summary, this section analyzed the behavior of three important parameters to be regarded in CO_2 storage operations in NFR's: $V^{\%}_{CO_2}$, $M^{\max}_{CO_2}$, and t_{95}. While the first two parameters are easily calculated using the rock and fluids properties, the drainage time scales were postprocessed from the numerical simulations. Since running fully resolved block simulations may be prohibitive for real formations, the development of an analytical estimate for t_{95}, the drainage time scale, is an important contribution of this work and is shown in the next sections.

3.3. Estimation of Drainage Time Scale From Fractional Flow

In this section, we investigate the saturation equation for incompressible two-phase flow (equation (2)) to develop a time scale estimate for the drainage process. We consider that drainage occurs essentially as a vertical downward displacement, as observed in experiments described by Pedrera et al. (2002) and Hagoort (1980), and later used by Di Donato et al. (2006) and March et al. (2017) to develop transfer functions for gravity drainage. Therefore, we rewrite equation (2) below assuming one-dimensional downwards displacement of the nonwetting phase and omitting the source terms:

$$\phi_m \frac{\partial S_w}{\partial t} = -\frac{\partial}{\partial z}\left(\overbrace{f_w}^{\Psi} q_t + \overbrace{k f_w \lambda_n \frac{dP_c}{dS_w}}^{\Pi} \frac{\partial S_w}{\partial z} + \overbrace{k f_w \lambda_n \Delta\rho g}^{\Gamma} \right). \tag{4}$$

We note that the groups Ψ, Π, and Γ are functions of the saturation only apart from $q_t = q_t(t)$ and $\frac{\partial S_w}{\partial z}$, which are nonlocal and depend on z and t. We estimate $\frac{\partial S_w}{\partial z} \approx \frac{\Delta S_w}{H}$ and assume that we can find a suitable estimator for the total flux $q_t(t) \approx \overline{q_t}$. Given these approximations, the groups are a function of S_w only and the spatial differential is written as $\partial/\partial z = (\partial S_w/\partial z)(d/dS_w)$ via the chain rule. Hence, a time scale for the saturation change is estimated by linearizing each of the terms of equation (4):

$$\begin{aligned} \phi_m \Delta S_w \tilde{t} &\approx \frac{\Delta S_w}{H} \frac{d}{dS_w}\left(\overline{q_t}\Psi + \frac{\Delta S_w}{H}\Pi + \Gamma \right) \Rightarrow \\ 1\tilde{t} &\approx \frac{1}{\phi_m}\frac{1}{H}\left(\overline{q_t}\frac{d\Psi}{dS_w} + \frac{\Delta S_w}{H}\frac{d\Pi}{dS_w} + \frac{d\Gamma}{dS_w} \right), \end{aligned} \tag{5}$$

where ΔS_w is estimated by $\Delta S_w \approx 1 - S_{wr}$. H is the maximum penetration depth of CO_2 in the matrix block, that is, the depth inside the matrix block where the difference between the phase pressures of brine and CO_2 equals the capillary entry pressure. It is calculated as $H = L_z - P_e/(\Delta\rho g)$. This parameter is a natural length scale for the drainage process, as most of the drainage happens until the CO_2 front reaches this depth. This approach follows the developments of Di Donato et al. (2006), but with a key difference regarding the assumptions about the fluid properties: Di Donato et al. (2006) assume that $\mu_w \gg \mu_n$, which reduces the equation to a form that does not include the group Ψ and where the groups Π and Γ do not include the mobility of the nonwetting phase (λ_n); this assumption is not valid for CO_2-brine systems. We have shown in the last section that in some scenarios relevant to CO_2 storage applications the wetting phase properties do alter the behavior of the drainage process. Therefore, we do not make any assumptions regarding the fluid properties and aim to derive a general estimate of the time scale for any set of properties. The saturation derivatives in equation (5) are estimated by considering the maximum of each group over the saturation range as a characteristic value. We therefore write:

$$\frac{d\Psi}{dS_w} \approx \frac{\max_{S_w}(\Psi)}{\Delta S_w}, \tag{6}$$

$$\frac{d\Pi}{dS_w} \approx \frac{\max_{S_w}(\Pi)}{\Delta S_w}, \tag{7}$$

$$\frac{d\Gamma}{dS_w} \approx \frac{\max_{S_w}(\Gamma)}{\Delta S_w}. \tag{8}$$

To close the model, a characteristic value for $\overline{q_t}$ is needed. We note that the total flux is constant in z but changes over time. It is highest at the onset of the drainage process and approaches zero when drainage is finished. We therefore use the maximum total flux to provide an estimate to q_t ($\overline{q_t} = q_t(0)$). Isolating q_t in equation (2), integrating in space and assuming hydrostatic pressure in the nonwetting phase at the boundaries, we obtain:

$$q_t(t) = \frac{1}{\int_0^{L_z} \frac{1}{k\lambda_t} dz}\left[-\rho_n g L_z - p_c(z=0) + \int_0^{L_z} f_w \rho_w g + f_n \rho_n g - \lambda_n \frac{\partial p_c}{\partial z} dz \right], \tag{9}$$

which gives us, assuming $S_w(z, t=0) = 1$:

$$\overline{q_t} = q_t(t=0) = \frac{k k_{rw}^{\max}}{L_z \mu_w}(\Delta\rho g L_z - p_c(z=0)). \tag{10}$$

The capillary pressure at the top of the domain can be estimated by considering a high value of brine saturation, say $S_w = 0.9$, noting that at the onset of the drainage process only a small amount of nonwetting phase will have invaded the domain. The total flux estimate closes the model, and its performance will be assessed by using it in a transfer function that is tested against the high-resolution simulations described in the previous section. The evaluation of the saturation-dependent functions at their maximum may lead to an over-estimation of the transfer rate for some cases, particularly in the late-time regime of the drainage process. However, as shown in section 3.5, the transfer function that is developed in the next section using this time scale predicts with good accuracy the drainage of the blocks for a large part of the drainage time.

3.4. Development of a New Transfer Function for CO_2 Gravity Drainage

Most commercial simulators (e.g., Computer Modelling Group, 2016; Schlumberger, 2014) and scientific publications (e.g., Ahmed Elfeel et al., 2016; Al-Kobaisi et al., 2009; Bech et al., 1991; Beckner et al., 1991) rely on the work of Gilman (1986) to model gravity-induced drainage transfer functions $\{T_w, T_n\}$ (equation (3)), sometimes applying a discretization of the matrix blocks (Beckner et al., 1991; Pruess, 1985). These transfer functions model the matrix-fracture flow as proportional to the potential difference between the two continua. Mathematically, this translates to:

$$\begin{aligned} T_n &= \sigma \frac{k_m k_{rn}}{\mu_n}\left(p_n^f - p_n^m + \Delta\rho(h_n^f - h_n^m) g \frac{L_z}{2}\right), \\ T_w &= \sigma \frac{k_m k_{rw}}{\mu_w}\left(p_w^f - p_w^m - \Delta\rho(h_n^f - h_n^m) g \frac{L_z}{2}\right), \end{aligned} \tag{11}$$

where σ is the shape factor, that accounts for the matrix area that is open for flow, k_m is the permeability of the matrix and $k_{r\alpha}$ are the relative permeabilities, that are typically evaluated upstream. However, despite intuitive and simple to implement in a dual-porosity simulator, it has been noted by other authors (Abushaikha & Gosselin, 2008; Ramirez et al., 2009) that this model fails to capture gravity drainage processes accurately, specifically if the blocks are tall. Moreover, it is important to note that the transfer functions defined by equation (11) do not converge to the correct limit $V_{CO_2}^{\max}$ as the transfer ceases, and will therefore over-estimate the final storage of CO_2 at the matrix-block scale. This is typically corrected using *pseudoization* techniques that adjust the final amount of nonwetting phase that drains the matrix, at the cost of misrepresenting the drainage dynamics even more (Abushaikha & Gosselin, 2008; Schlumberger, 2014). As shown later in this section, the mismatch between the storage results given by high-resolution block simulations and the results given by equation (11) are specially high when considering rock and fluid properties relevant to CO_2 storage applications.

The time scale $\tilde{t}$ defined in equation (5) is used to develop an improved transfer function that captures the dynamics of CO_2-induced gravity drainage. We start by defining the transfer rate coefficient β as:

$$\beta = \frac{1}{\tilde{t}}. \tag{12}$$

We then use β on an exponential model, as initially proposed by Aronofsky et al. (1958) and later on used by Kazemi et al. (1992), Schmid and Geiger (2012), and Schmid and Geiger (2013) to model spontaneous imbibition and by Zhou et al. (2017) to model diffusive transfer of CO_2 in fractured reservoirs. We therefore write the relative transfer of CO_2 to the matrix by gravity drainage as:

$$\frac{V_{CO_2}(t)}{V_{CO_2}^{\max}} = 1 - e^{-t/\tilde{t}} \equiv 1 - e^{-\beta t}. \tag{13}$$

Differentiation of this expression with respect to time and multiplication by a smooth activation function $F(S_{nf})$ leads to:

$$\phi_m \rho_{nm} \frac{\partial S_{nm}}{\partial t} = T_n = \phi_m \rho_{nm} \beta F(S_{nf})\left(S_{nm}^{\max} - S_{nm}\right), \tag{14}$$

where $S_{nm}^{\max}$ is the average saturation corresponding to the maximum volume of CO_2 a block can store. The activation function ensures a smooth activation of the transfer only when CO_2 is available in the fracture cell. It is defined (Lu et al., 2008) as:

$$F(S_{nf}) = \frac{1 - e^{-\sqrt{k_f^*/k_m} S_{nf}}}{1 - e^{-\sqrt{k_f^*/k_m}}}, \tag{15}$$

where k_f^* is a measure of the permeability in the fracture cell, taken here as $\max\{k_{fx}, k_{fy}, k_{fz}\}$. The activation function ensures the transfer starts when the fractures are saturated by CO_2. The transfer ceases exactly when the block is saturated by the maximum amount of CO_2. It is important to emphasize that a general assumption of transfer functions like the one defined above is that all the matrix blocks within a simulation grid block are similar and are surrounded by CO_2 once the plume arrives at this point. This is a common assumption done in the derivation of transfer functions for dual-porosity models, that is particularly reasonable when the vertical dimensions of the block are larger than the horizontal ones, such as in the In Salah CO_2 storage project (Eiken et al., 2011; Iding & Ringrose, 2010).

As phases are assumed incompressible, summation of the phase equations in the matrix (last two equations of (3)) leads to $T_w = -T_n$. We note that this expression is very similar to the one suggested by Di Donato et al. (2006), but with a different transfer rate coefficient (parameter β). Di Donato et al. (2006) suggest the calculation of β as:

$$\beta = \left(\frac{1}{n_w}\right)\omega_g + (r-1)\omega_c, \tag{16}$$

where r is the gravity/capillary ratio, given by $r = \Delta\rho g L_z / P_e$, and ω_g and ω_c are characteristic time scales for gravity and capillary forces, given by $\omega_g = (k k_{rw}^{\max} \Delta\rho g)/(\phi_m H)$ and $\omega_c = (k k_{rw}^{\max} n_p P_e)/(\phi_m H^2)$. The $(1/n_w)$ and $(r-1)$ factors multiplying each time scale were derived empirically by matching the transfer expression to high-resolution one-dimensional block simulations. We note that the expression derived in this work contains no parameters that were fitted to numerical simulations, in contrast to other approaches.

3.5. Evaluation of Transfer Functions

Figures 4a and 5a show a comparative analysis between the transfer model proposed in this work and the one proposed by Gilman (1986). The curves corresponding to the latter were generated by running a 0-D dual-porosity model of single fracture and matrix cells, and tracking the saturation of CO_2 in the matrix block over time. No correction of the final volume of CO_2 in the block was applied here; the transfer is implemented as shown in equation (11). For the sugar cube geometry (Figure 4a), each case has the same position as

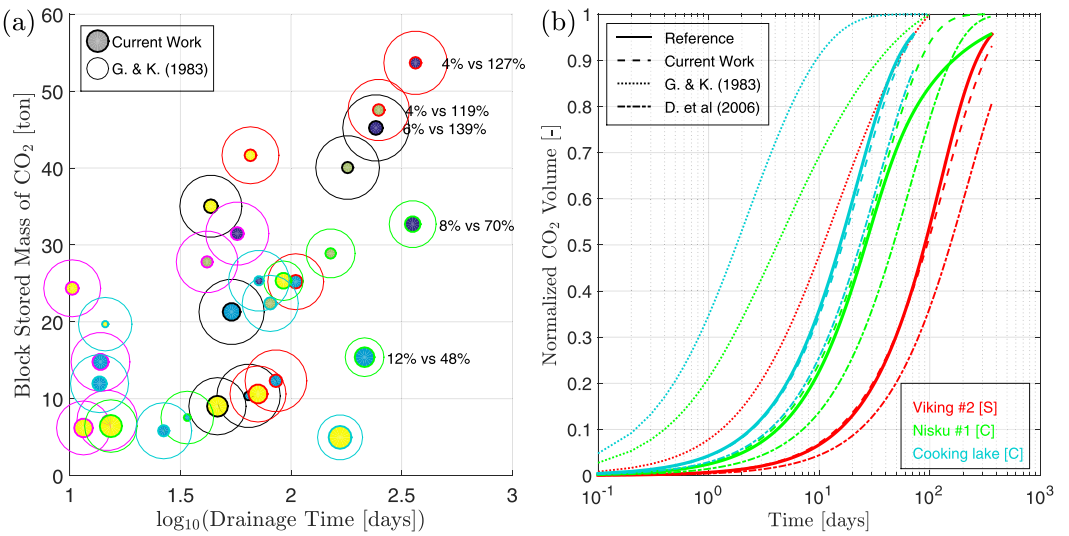

Figure 4. Evaluation of transfer functions for the sugar cube matrix geometry. Circles edges and fills are colored following the pattern in Figure 3. (a) The size of the circle is proportional to the error when using Gilman (1986) (nonsolid circles) and the transfer function proposed in this work (solid circles) to model the drainage process, relative to the 3-D numerical model. (b) Representative drainage curves showing the reference solution, given by high-resolution simulations of a single block (solid lines), the Gilman (1986) transfer function (dotted line), the Di Donato et al. (2006) transfer function (dash-dotted line) and the transfer function proposed in this work.

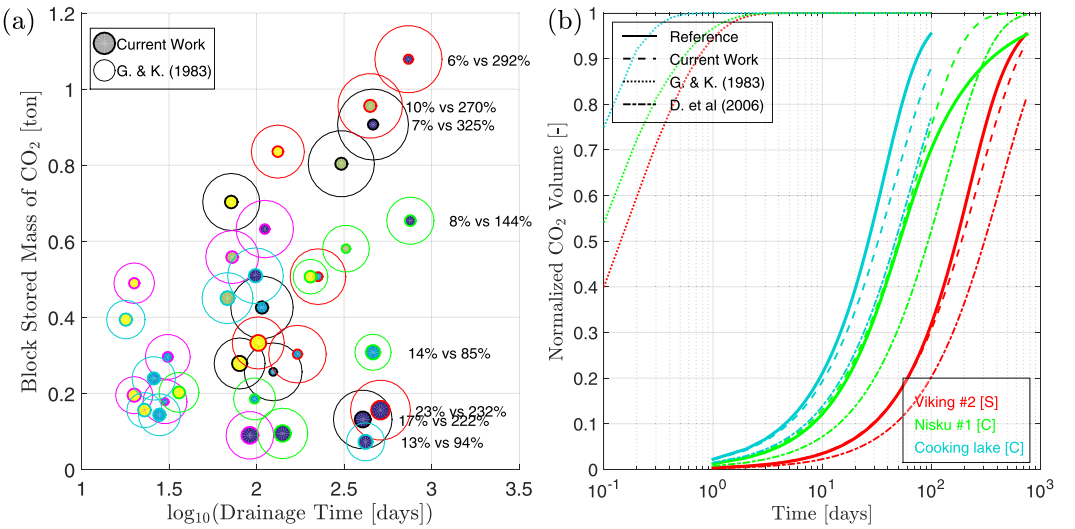

Figure 5. Evaluation of transfer functions for the match stick matrix geometry. Circles edges and fills are colored following the pattern in Figure 3. (a) The size of the circle is proportional to the error when using Gilman (1986) (nonsolid circles) and the transfer function proposed in this work (solid circles) to model the drainage process, relative to the 3-D numerical model. (b) Representative drainage curves showing the reference solution, given by high-resolution simulations of a single block (solid lines), the *Gilman* [1986] transfer function (dotted line), the *Di* Donato et al. (2006) transfer function (dash-dotted line) and the transfer function proposed in this work.

in Figure 3, but the circles are now scaled by the relative integral error of the transfer model defined by equation (13). The same applies for the match stick geometry. The relative integral error is defined as $E_{model} \equiv \int |I_{num} - I_{model}| dlogt / \int I_{num} dlogt$, where I_α is the normalized stored volume of CO_2 for the model α. Graphically, for each model, E_{model} represents the ratio between the area between the model and numerical curves and the area below the numerical curve in Figures 4b and 5b. For $E_{model} = 0$, the match is perfect. The error of Gilman's expression is represented as empty circles in the same positions of the solid circles, and also scaled by E_{model}. Actual error values are shown in the figure for the cases with high t_{95} in the plot for reference. For the color pattern used to identify each circle on the chart, please refer to Figure 3.

Figures 4a and 5a show that the model proposed in equation (13) provides much more accurate results compared to the one given by equation (11) for all cases (solid circles are always inside the empty circles). This is especially true for the match stick cases, which consist of fracture geometries extremely favorable to storage. The transfer model given by equation (11) misrepresents the storage dynamics by a factor as high as $\approx$ 325% for the match stick geometry and $\approx$ 139% for the sugar cube geometry, both for the cardium#2-shallow-cold-low-P_c case. The maximum error incurred by the proposed model is $\approx$ 23% for the match stick geometry (viking#2-shallow-cold-high-P_c case) and $\approx$ 16% for the match stick geometry (cooking-lake-deep-warm-high-P_c case). The best results are achieved for the high-storage cases (top part of the chart in Figures 4a and 5a). Figures 4b and 5b show representative storage curves for some high-storage cases. In these plots, the model of Di Donato et al. (2006) is also shown. The proposed model (dashed lines) seems to represent, with good accuracy, the whole extent of the drainage dynamics for most of the cases. The nisku#1 cases have a higher value of the Corey exponent (n_w=2.8). This induces longer late-time storage dynamics (the proposed model over-estimates storage at late time for the green curves). However, most of the transient dynamic is captured even for these cases. The model of Di Donato et al. (2006)—despite improving drastically over the one proposed in Gilman (1986)—appears to underestimate the storage for all the cases. We believe this is directly linked to neglecting the viscous time scale (first term of equation (5)), as the work of Di Donato et al. (2006) was focused on oil-gas systems, assuming $\mu_w \gg \mu_n$. The proposed model shows smaller errors for all cases when compared to the work of Di Donato et al. (2006). For all cases, Gilman (1986) over-estimates the transfer rate by several orders of magnitude and fails to represent the drainage process with any accuracy. This error is particularly high for match stick geometries, where the time to reach maximum recovery shows a difference that can reach the order of magnitude of a thousand days when compared to the high-resolution simulations. These results were also observed by Abushaikha

and Gosselin (2008). The results shown in this section provide an indication that our new model can be successfully used to model CO_2 storage in NFRs.

4. Field-Scale Considerations

The previous sections have focused on the storage of CO_2 at the scale of a matrix block. The negative impact of fractures on storage is summarized in Figure 3b, which shows the percentage of volume (or mass, as we consider incompressibility of CO_2 in supercritical state) that is lost when a system of interconnected fractures is present in the formation. This figure shows that fractures can reduce the CO_2 storage in a single block to values as low as 5% of the effective pore volume. This happens because a matrix block surrounded by CO_2 will be drained just until capillary and gravity forces balance. There are cases, however, in which good storage performance can be achieved, particularly for low capillary pressure levels and for warm basins. This static analysis show that a reasonable amount of CO_2 may be stored in a fractured reservoir depending on the geological environment.

Another aspect of concern regarding CO_2 storage in NFRs is the fate of the CO_2 plume. Since fractures have typically conductivities that are orders of magnitude higher than that of the rock matrix, it is usually speculated whether injected CO_2 may quickly flow through the fracture system without a significant volume of it being transferred to the rock matrix. We investigate the impact of fractures at the field scale by running two-dimensional simulations of CO_2 injection in a conceptual anticline geometry. We first compare the results of injection of a certain amount of CO_2 in a unfractured formation with the injection of the same amount in a formation that has the same properties of the rock matrix, but shows the presence of an interconnected fracture system. We then investigate why and how CO_2 injection rates should be limited in order to avoid the spilling of CO_2 through the fracture system without allowing for transfer to the matrix.

4.1. Setup of the Numerical Simulation Experiments

The numerical experiments shown hereafter correspond to CO_2 injection in the geometry representing a symmetric anticline, as shown in in Figure 6. The anticline dips at $\approx 2.8°$ (25 m/500 m). A well that is completed over the entire thickness of the formation ($L_z = 100$ m) injects CO_2 at rates that will be specified for each experiment. No-flow boundary conditions are considered at the top and bottom of the model, representing a cap rock and an underlying nonpermeable formation. We consider the lateral boundaries open for flow and at hydrostatic pressure of the resident fluid, which is brine. Simulations are carried out using MRST (Lie et al., 2011). The corner-point grid structure is used to discretize the domain. $N_x = 101$, $N_y = 1$, and $N_z = 100$ blocks are used for all the simulations (the extra block in x direction is used to ensure symmetry of the grid).

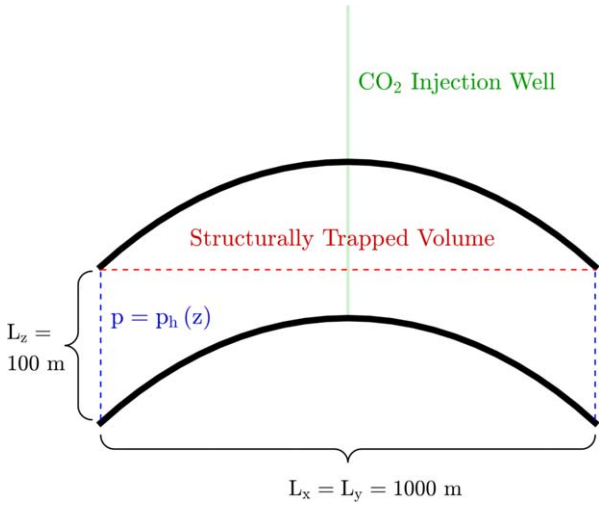

Figure 6. Conceptual picture of the anticline geometry considered for the simulations in section 4. CO_2 is injected on a well completed over the entire thickness of the anticline (green line). Injected CO_2 is structurally trapped only in the upper portion of the anticline, between the dashed red line and the cap rock. Lateral faces are open for flow, and hydrostatic pressure of brine is assigned to these faces. No-flow boundary conditions are considered for the top and bottom boundaries, representing the overburden and underburden to the aquifer. Note that the picture is vertically exaggerated and the dip of the anticline is not to scale.

The fracture system is represented as a homogeneous medium with no capillary pressure and each fracture cell has a porosity of $\phi_f = 0.01$ (Firoozabadi & Thomas, 1990). No residual saturations and quadratic relative permeabilities are assumed for the fracture system (Rossen & Kumar, 1992). The absolute permeability of the fracture system is set to be anisotropic: $k_{fx} = 405$ mD and $k_{fz} = 4053$ mD, corresponding to a nearly vertical set of fractures. These are realistic values taken from the In Salah Gas Joint Venture CO_2 storage project (Cavanagh & Ringrose, 2011) and were found via discrete fracture network (DFN) modeling (Iding & Ringrose, 2010). Four cases are considered in the forthcoming analysis. Two cases with high drainage times (viking#2-shallow-cold-low-P_c and cardium#2-deep-warm-low-P_c) and two further cases with low drainage times (nisku#1-shallow-cold-low-P_c and cooking-lake-shallow-warm-high-P_c). These cases define the rock properties for the unfractured simulations and β and S_{nm}^{max} for the dual-porosity simulations (see Table 2 for a summary of the selected cases).

Table 2
Summary of the Selected Cases for the Field-Scale Simulations

Case	β (1/s)	S_{nm}^{max} (–)	q_{num} (m^3/d) (ideal value-numerical)	q_{inj}^{max} (m^3/d) (equation (17))	q_{inj}^{max}/q_{num}
viking#2	8.48×10^{-8}	0.39	894	3,499	≈ 4
nisku#1	3.22×10^{-7}	0.45	1,158	8,068	≈ 7
cooking-lake	1.99×10^{-6}	0.21	5,406	23,270	≈ 4
cardium#2	6.03×10^{-7}	0.45	4,634	24,175	≈ 5

4.2. Impact of Fractures in the Field-Scale Storage of CO_2

Figure 7 shows a comparison of CO_2 storage in fractured and unfractured formations. As the existence of a fracture system may not be known in advance, we aim at understanding how an operation that was designed for a unfractured formation would be affected by the presence of fractures. This situation occurred in the In Salah Project, where the existence of a fracture system was not recognized before the injection started (Iding & Ringrose, 2010). Hence, we compare the results of CO_2 injection in a fractured formation, using the dual-porosity model developed in section 3.4, with the injection in an unfractured formation. In our simulations, a volume equal to the effective pore volume available for safe storage on the structural trap, PV^{eff}, (see Figure 6) is injected over 1,000 days. After this time, injection ceases as further injection would cause CO_2 to spill through the boundaries, even without the presence of fractures.

Figures 7a and 7b show the CO_2 saturation fields at $t = 1{,}000$ days before injection ceases for the fractured and unfractured simulations, respectively. A well-developed plume is seen in the unfractured simulation, while in the fractured case, the presence of a high-permeability fracture system induces the quick segregation of CO_2 at the top of the fractures. The transfer to the matrix takes time. The time scale is determined by the transfer rate coefficient β (see equation (13)). Figure 7c shows the mass of CO_2 in the system for the fractured and unfractured models. We note a decrease of $\approx$ 27% in the stored CO_2 volume when fractures are added to the system. If the CO_2 that is stored in the matrix (dashed line) is compared to the case where the fractures are absent (solid blue line), the difference ($\approx$ 32%) corresponds precisely to $100\%-V_{CO_2}^{\%}$ (see

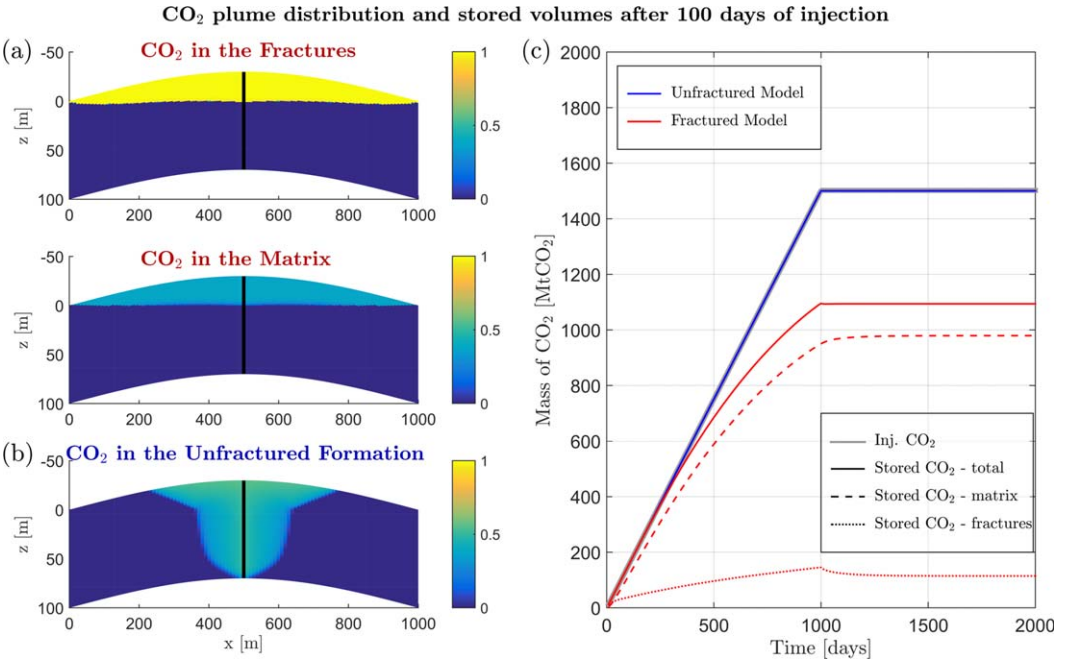

Figure 7. CO_2 saturation distributions for the viking#2-shallow-cold-low-P_c properties, for (a) the fractured anticline (top fractures, bottom matrix) and (b) the unfractured anticline. (c) Injected and stored mass of CO_2 for both simulation cases. Storage efficiency is reduced in the fractured case, and CO_2 escapes through the boundaries (solid red line diverging from thick gray line at $\approx$ 400 days), reflecting the fast flow of CO_2 through the fracture system.

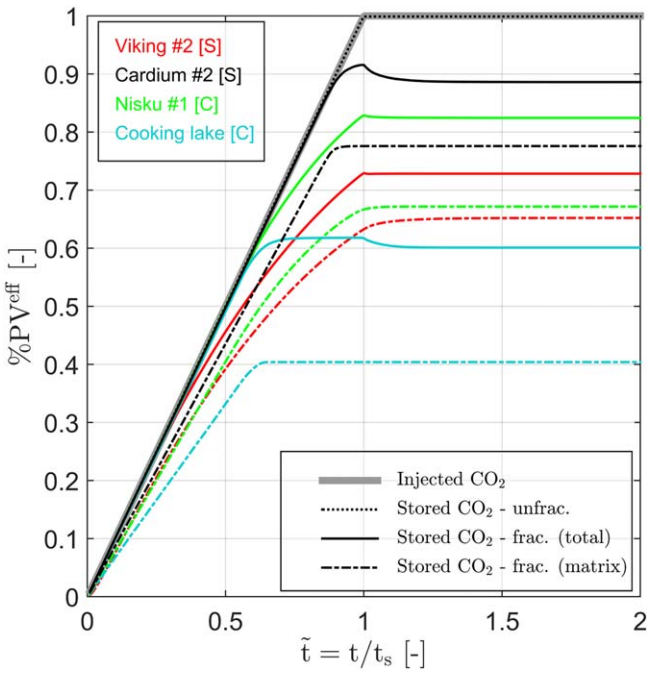

Figure 8. Relative injected and stored volumes for the field-scale simulations. Time is normalized by 1,000 days, when injection stops. Solid lines represent the total volume of CO_2 stored in the fractured anticlines, while dotted lines represent the total volume of CO_2 stored in the corresponding unfractured model. The difference between both curves shows the reduction in storage efficiency loss when a system of connected fractures exists in the formation.

section 3.2 and Figure 3b). Therefore, since most of the CO_2 is stored in the matrix, $V^{\%}_{CO_2}$ may be used as a correction factor for volumetric CO_2 storage estimates, at least as a first-order approximation. This is more evident in Figure 8, where we plot the injected volume normalized by the effective pore volume (PV^{eff}). CO_2 in the matrix (dash-dotted lines) match $V^{\%}_{CO_2}$ approximately, as explained above. The difference between the solid curves and the thick gray line represents the amount of CO_2 that left the system through the boundaries, i.e., spilling the anticline through the top corners of the model. An ideal operation would ensure that all the injected CO_2 remains in the domain, where it can be safely trapped. The spill times depend not only on ρ_α, injection rate and thickness of the formation (which determines the shape of the plume in the fracture system) but also on the transfer rate β and S^{max}_{nm}. Compare, for instance, the viking#2 and nisku#1 cases, that correspond to the same environment (shallow-cold). If there was no transfer, the stored CO_2 for these two cases should be the same, as the rock and fluid properties would be the same. However, because the transfer dynamics is faster for the nisku#1 case (see Figure 4b), injected CO_2 is transferred faster to the matrix, avoiding the early spill time seen in the viking#2 case. There is, in fact, an optimal injection rate that avoids spilling if the correct amount of CO_2 is injected for each case. This topic is approached in the next section.

4.3. Injection Rate Considerations

We now explore aspects regarding injectivity of CO_2 in NFRs. We disregard the injection rate limitations imposed by the integrity of the cap rock in this analysis, noting that the fractures will allow for higher injectivity compared to an unfractured formation. We now inject the maximum amount of CO_2 that the matrix can store for each case, which is given by $V_{inj} = S^{max}_{nm} \phi_m V_a$, where V_a is the volume of the anticline (the volume of the formation above the red dashed line in Figure 6). We consider three different injection rates: $V_{inj}/(1,000$ days), $V_{inj}/(500$ days), and $V_{inj}/(100$ days). The results are summarized in Figure 9. We focus the discussion, initially, in Figure 9a. The difference between injected CO_2 (solid line) and stored CO_2 (dashed line) is the amount of CO_2 that spilled. We note that all three initial injection rates (blue, red, and black lines) are high enough so that CO_2 travels quickly through the fracture system without allowing for enough time to transfer to the matrix. If the injection rate is reduced to $V_{inj}/(1,600$ days) (magenta curve), the injected CO_2 is safely trapped in the anticline. The same procedure is applied to the other three cases to reveal the injection rates that minimize the spilled CO_2. As mentioned in the previous section, one must be more conservative regarding the injection rate for the low β cases (viking#2 and nisku#1). Ideal injection rates are, in fact, monotonically increasing with β.

The following simple model serves as an estimation of the maximum injection rate in NFRs:

$$q^{max}_{inj} = \frac{V_{inj}}{t_{95}}. \tag{17}$$

This model implies that one should inject at a rate that is no higher than the maximum amount one can store in the rock matrix divided by the time it takes to saturate 95% of the matrix pore volume. t_{95} may be easily calculated by inverting equation (13) and evaluating it for $V_{CO_2}(t)/V^{max}_{CO_2} = 0.95$. Although this model has some physical reasoning behind it, it lacks a fundamental component for a more accurate estimate, which is the geometrical component of the CO_2 plume in the fracture system. Table 2 shows a summary of the injection rates found via numerical simulation and using the model given by equation (17). We define the accuracy factor of the injection rate estimate as q^{max}_{inj}/q_{num}, where q_{num} is the optimal injection rate obtained from numerical simulations (magenta curves in Figure 9). The accuracy factor ranges from ≈ 4 to ≈ 7. This model, despite simple, provides an order-of-magnitude estimate of the optimal injection rate. It should be noted that the accuracy factors are overestimated with the 2-D numerical simulations carried in

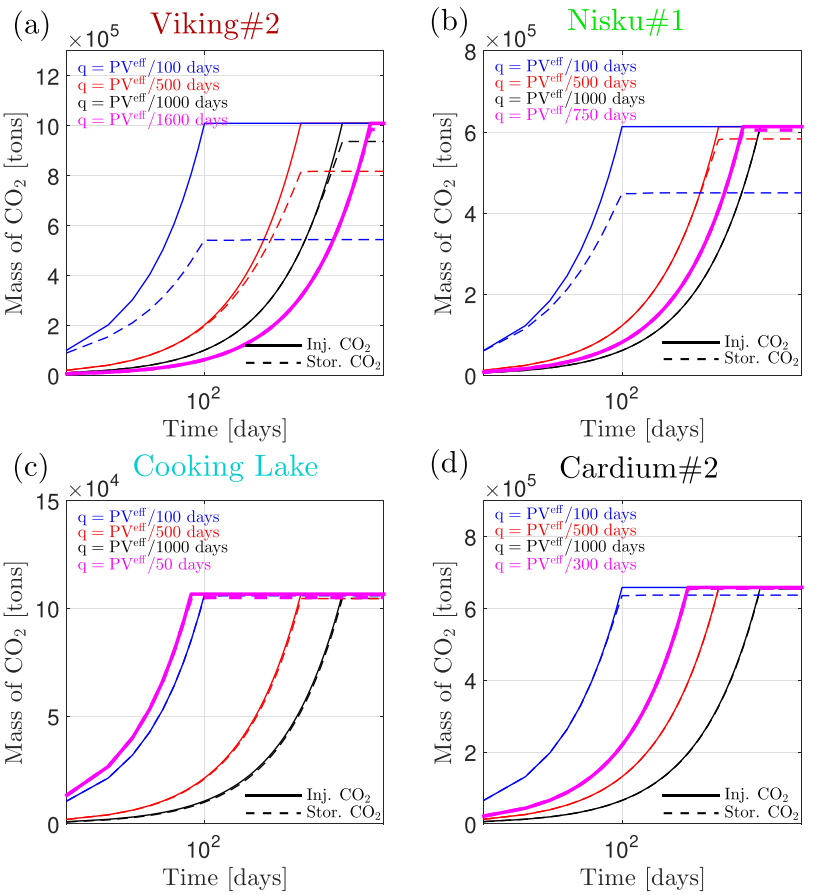

Figure 9. Injected (solid lines) and stored mass (dashed lines) of CO_2 for (a) viking#2, (b) nisku#1, (c) cooking-lake, and (d) cardium#2 cases in the geometry depicted in Figure 6. Each case has its "optimal" injection rate, i.e., an injection rate that minimizes spilling of CO_2.

this section. The consideration of a third dimension in the *y* direction would lead to a higher q_{num}, making this value closer to the proposed model given by equation (17). This gives us indications that this model could serve as a good initial indicator of the magnitude of the injection rate that avoids the early spill of CO_2 for anticlines.

5. Summary and Conclusions

Carbon capture and storage (CCS) is a promising technique to reduce the concentration of greenhouse gases in the atmosphere. Fractured reservoirs are ubiquitous across the world. A large percentage of the world's hydrocarbon resources come from naturally fractured reservoirs, that could be later used for CO_2 storage. However, fractured reservoirs are not typically considered as formations with potential to safely store CO_2. The main concerns regarding storage in fractured formations are the high conductivity of the fracture system, that may lead to lost control of the CO_2 plume and capillary forces that will tend to keep CO_2 outside the unfractured rock matrix.

Simulating the dynamics in naturally fractured reservoirs is a complex and computationally intensive task, as there are several mechanisms by which fractures and matrix exchange fluids. Moreover, fractures introduce a new time scale to fluid flow, as the transfer to the matrix will typically be much slower than the flow in the fractures. Yet, numerical simulations are extremely useful to obtain insights about the reservoir dynamics during CO_2 storage in fractured formations. To simplify the computational system, dual-porosity models have been used for many years due to their simplicity and computational efficiency, as they upscale the transfer behavior and average properties of the fracture system. A fundamental ingredient of dual-

porosity models are transfer functions that describe the fluid exchange rate between fractures and matrix. Currently existing transfer functions are designed for oil-gas systems, and fail to represent the dynamics of drainage induced by supercritical CO_2. Therefore, one of the key contributions of this work was the development of a new transfer function that models CO_2-induced gravity drainage accurately. This transfer function is based on a time scale analysis of the physics of immiscible multiphase flow combined with an exponential model, as suggested initially by Di Donato et al. (2006). A more formal treatment of each time scale term, combined with the inclusion of the viscous term, improves the original model of Di Donato et al. (2006) and the widely used model of Gilman (1986). Our new model requires no fitting to numerical simulations, is consistent and captures the drainage process accurately. The transfer function presented here is easy to implement in any dual-porosity simulator.

At the matrix-block scale, we show that the percentage of the matrix-block volume that is effectively used for storage is higher for deep formations in cold basins and lower for shallow formations in warm basins ($\approx$ 40% versus $\approx$ 15%). In contrast to this result, deep formations in cold basins will lead to a higher mass of CO_2 stored per unit volume, due to the high density of the supercritical fluid. This indicates a competing behavior of CO_2 density in fractured reservoirs: for a fixed brine density ρ_b, a high value of ρ_c increases the stored mass per unit volume, but decreases the stored mass on each block due to the decreased density difference $\Delta\rho$. Our studies show that in a shallow formation in a warm basin the negative impact of fractures on the storativity of CO_2 is less pronounced. Therefore, in such formations, the existence of an interconnected system of fractures would not grossly impact the final storage.

At the field scale, we have shown that the injection rate for a fractured anticline must be designed to avoid what is termed here as "early spill": the fast flow of CO_2 through the fracture system without significant storage in the matrix. We have shown that the spill time for a conceptual anticline geometry is heavily dependent on the transfer rate between the two continua. An initial model to estimate the order of magnitude of the ideal injection rate is proposed (equation (17)). Numerical experiments shown in Figure 9 indicate that this model captures the order of magnitude of the optimal injection rate that avoids early spill, even though it does not consider the geometrical aspect of the CO_2 plume in the fracture system. Although we understand that the major injection rate design criteria for CO_2 storage is still the integrity of the sealing formation, we point out in this work that a new aspect of injection rate determination must be taken into consideration when using an NFR for storage.

General guidelines for CO_2 storage in NFRs include:

1. The correction of storage estimates to account for a loss in storativity caused by the presence of a fracture system.
2. The use of numerical simulations with the transfer function developed here to evaluate the spill time and to design an optimal injection plan for the fractured aquifer. The model given by equation (17) gives an order of magnitude of this injection rate, but must be used with caution as it does not consider geometrical aspects of the formation.

Although this work consists of a simplified first-order physics analysis, we believe it is an important initial step in the analysis of CO_2 storage in NFRs, which, in principle, could be used for CO_2 storage if the geological conditions are right and the injection rates are managed appropriately.

Acknowledgments
This material is based upon work supported by the U.S. Department of Energy (DOE) National Energy Technology Laboratory (NETL) under grant FE0023323. This project is managed and administered by Princeton University and funded by DOE/NETL and cost-sharing partners. Neither the United States Government nor any agency thereof, nor any of their employees, makes any warranty, express or implied, or assumes any legal liability or responsibility for the accuracy, completeness, or usefulness of any information, apparatus, product, or process disclosed, or represents that its use would not infringe privately owned rights. Reference herein to any specific commercial product, process, or service by trade name, trademark, manufacturer, or otherwise does not necessarily constitute or imply its endorsement, recommendation, or favoring by the U.S. Government or any agency thereof. The views and opinions of authors expressed herein do not necessarily state or reflect those of the U.S. Government or any agency thereof. The authors also thank the financial support provided by Energi Simulation for supporting Sebastian Geiger's Chair for Carbonate Reservoir Simulation and the reviewers for the insightful comments that helped improving this work. All data for this paper are properly cited and referred to in the reference list. Simulations were carried out with the open-source code MRST, and the related Matlab scripts are available online at the Software section of the website http://carbonates.hw.ac.uk.

References

Abushaikha, S. A. A., & Gosselin, O. R. (2008). Matrix-fracture transfer function in dual-medium flow simulation: Review, comparison, and validation (SPE 113890). In *2008 SPE Europec/EAGE annual conference and exhibition*, Rome, Italy, 9–12 June.

Agada, S., Geiger, S., & Doster, F. (2016). Wettability, hysteresis and fracture-matrix interaction during CO_2 EOR and storage in fractured carbonate reservoirs. *International Journal of Greenhouse Gas Control*, *46*, 57–75.

Ahmed Elfeel, M., Al-Dhahli, A., Geiger, S., & van Dijke, M. I. (2016). Fracture-matrix interactions during immiscible three-phase flow. *Journal of Petroleum Science and Engineering*, *143*, 171–186.

Al-Kobaisi, M., Kazemi, H., Ramirez, B., Ozkan, E., & Atan, S. (2009). A critical review for proper use of water/oil/gas transfer functions in dual-porosity naturally fractured reservoirs: Part II (SPE 124213). *SPE Reservoir Evaluation and Engineering*, *12*, 211–217.

Aronofsky, J. S., Masse, L., & Natanson, S. G. (1958). A model for the mechanism of oil recovery from the porous matrix due to water invasion in fractured reservoirs. *SPE Journal*, *213*(2), 2–4.

Bear, J. (1972). *Dynamics of fluids in porous media*. New York, NY: American Elsevier Publishing Company.

Bech, N., Jensen, O., & Nielsen, B. (1991). Modeling of gravity-imbibition and gravity-drainage processes. *SPE Journal*, *6*(1), 129–136.

Beckner, B., H., Chan, A., McDonald, S. Wooten., & Jones, (1991). Simulating naturally fractured reservoirs using a subdomain method (SPE 21241). In *11th SPE symposium on reservoir simulation*, Anaheim, USA, 17–20 February.

Bennion, D. B., & Bachu, S. (2006). Supercritical CO_2 and H_2S brine drainage and imbibition relative permeability relationships for intergranular sandstone and carbonate formations (SPE 99326). In *2006 SPE Europec/EAGE annual conference and exhibition*, Vienna, Austria, 12–15 June.

Bennion, D. B., & Bachu, S. (2008). Drainage and imbibition relative permeability relationships for supercritical CO_2/brine and H2S/brine systems in intergranular sandstone, carbonate, shale, and anhydrite rocks. *SPE Reservoir Evaluation and Engineering*, *11*, 487–496.

Bourbiaux, B. J., Basquet, R., Cacas, M-C., Daniel, J-M., & Sarda, S. (2002). An integrated workflow to account for multi-scale fractures in reservoir simulation models: Implementation and benefits (SPE 78489). In *10th Abu Dhabi international petroleum exhibition and conference*, 13–16 October 2002.

Burchette, T. P. (2012). Carbonate rocks and petroleum reservoirs: A geological perspective from the industry. *Geological Society, London, Special Publications*, *370*, 17–37.

Cavanagh, A., & Ringrose, P. (2011). Simulation of CO_2 distribution at the In Salah storage site using high-resolution field-scale models. *Energy Procedia*, *4*, 3730–3737.

Celia, M. A., Bachu, S., Nordbotten, J. M., & Bandilla, K. W. (2015). Status of CO_2 storage in deep saline aquifers with emphasis on modeling approaches and practical simulations. *Water Resources Research*, *51*, 6846–6892. https://doi.org/10.1002/2015WR017609

Computer Modelling Group Ltd (2016). IMEX User Guide - Three-phase Black-Oil Reservoir Simulator Version 2016.

Cuellar-Franca, R. M., & Azapagic, A. (2015). Carbon capture, storage and utilisation technologies: A critical analysis and comparison of their life cycle environmental impacts. *Journal of CO2 Utilization*, *9*, 82–102.

Di Donato, G., Lu, H., Tavassoli, Z., & Blunt, M. J. (2007). Multirate-transfer dual-porosity modeling of gravity drainage and imbibition (SPE 93144). *SPE Journal*, *12*, 77–88.

Di Donato, G., Tavassoli, Z., & Blunt, M. J. (2006). Analytical and numerical analysis of oil recovery by gravity drainage. *Journal of Petroleum Science and Engineering*, *54*(1–2), 55–69.

Egya, D. O., Geiger, S., Corbett, P. W. M., March, R., Bisdom, K., Bertotti, G., et al. (2018). Analysing the limitations of the dual-porosity response during well tests in naturally fractured reservoirs. *Petroleum Geoscience*. https://doi.org/10.1144/petgeo2017-053

Eiken, O., Ringrose, P., Hermanrud, C., Nazarian, B., Torp, T. A., & Høier, L. (2011). Lessons Learned from 14 years of CCS Operations: Sleipner, In Salah and Snohvit. *Energy Procedia*, *4*, 5541–5548.

Emami-Meybodi, H., & Hassanzadeh, H. (2015). Advances in water resources two-phase convective mixing under a buoyant plume of CO_2 in deep saline aquifers. *Advances in Water Resources*, *76*, 55–71.

Fernø, M., Haugen, Å., Wickramathilaka, S., Howard, J., Graue, A., Mason, G., et al. (2013). Magnetic resonance imaging of the development of fronts during spontaneous imbibition. *Journal of Petroleum Science and Engineering*, *101*, 1–11.

Firoozabadi, A., & Thomas, L. K. (1990). Sixth SPE comparative solution project: Dual-porosity simulators. *Journal of Petroleum Technology*, *42*(6), 710–763.

Fumagalli, A., Pasquale, L., Zonca, S., & Micheletti, S. (2016). An upscaling procedure for fractured reservoirs with embedded grids. *Water Resources Research*, *52*, 6506–6525. https://doi.org/10.1002/2015WR017729

Geiger, S., Dentz, M., & Neuweiler, I. (2013). A novel multirate dual-porosity model for improved simulation of fractured and multiporosity reservoirs (SPE 148130). *SPE Journal*, *18*(4), 670–684.

Geiger, S., Matthai, S. K., Niessner, J., & Helmig, R. (2009). Black-oil simulations for three-component, three-phase flow in fractured porous media (SPE 107485). *SPE Journal*, *14*(2), 338–354.

Gilman, J. (1986). An efficient finite-difference method for simulating phase segregation in the matrix blocks in double-porosity reservoirs. *SPE Reservoir Engineering*, *1*(4), 403–413.

Guo, B., Bandilla, K. W., Doster, F., Keilegavlen, E., & Celia, M. A. (2014). A vertically integrated model with vertical dynamics for CO_2 storage. *Water Resources Research*, *50*, 6269–6284. https://doi.org/10.1002/2013WR015215

Hagoort, J. (1980). Oil recovery by gravity drainage. *SPE Journal*, *20*(3), 139–150.

Iding, M., & Ringrose, P. (2010). Evaluating the impact of fractures on the performance of the In Salah CO_2 storage site. *International Journal of Greenhouse Gas Control*, *4*(2), 242–248.

Intergovernmental Panel on Climate Change (IPCC) (2005). *Special report on carbon dioxide capture and storage*. Cambridge, UK: Cambridge University Press.

Juanes, R., Spiteri, E. J., Orr, F. M., & Blunt, M. J. (2006). Impact of relative permeability hysteresis on geological CO_2 storage. *Water Resources Research*, *42*, W12418. https://doi.org/10.1029/2005WR004806

Karimi-Fard, M., Durlofsky, L. J., & Aziz, K. (2004). An efficient discrete-fracture model applicable for general-purpose reservoir simulators (SPE 88812). *SPE Journal*, *9*(2), 227–236.

Kazemi, H., Gilman, J. R., & Eisharkawy, A. M. (1992). Analytical and numerical solution of oil recovery from fractured reservoirs with empirical transfer functions. *SPE Reservoir Engineering*, *7*(2), 219–227.

Kazemi, H., Merrill, L. Jr., Porterfield, K., & Zeman, P. (1976). Numerical simulation of water-oil flow in naturally fractured reservoirs (SPE 5719). *SPE Journal*, *16*(6), 317–326.

Labastie, A. (1990). Capillary continuity between blocks of a fractured reservoir (SPE 20515). In *65th SPE annual technical conference and exhibition*, New Orleans, USA, 23–26 September.

Law, D. H.-S., & Bachu, S. (1996). Hydrogeological and numerical analysis of CO_2 disposal in deep aquifers in the Alberta sedimentary basin. *Energy Conversion and Management*, *37*(6–8), 1167–1174.

Lemonnier, P., & Bourbiaux, B. J. (2010a). Simulation of naturally fractured reservoirs. State of the art—Part 2: Matrix-fracture transfers and typical features of numerical studies. *Oil & Gas Science and Technology Revue De L'Institut Francais Du Petrole*, *65*(2), 263–286.

Lemonnier, P., & Bourbiaux, B. J. (2010b). Simulation of naturally fractured reservoirs. State of the art—Part 1: Physical mechanisms and simulator formulation. *Oil & Gas Science and Technology Revue De L'Institut Francais Du Petrole*, *65*(2), 239–262.

Lie, K.-A., Krogstad, S., Ligaarden, I. S., Natvig, J. R., Nilsen, H. M., & Skaflestad, B. (2011). Open-source MATLAB implementation of consistent discretisations on complex grids. *Computational Geosciences*, *16*(2), 297–322.

Lu, H., Di Donato, G., & Blunt, M. J. (2008). General transfer functions for multiphase flow in fractured reservoirs (SPE 102542). *SPE Journal*, *13*(3), 289–297.

Macminn, C. W., Szulczewski, M. L., & Juanes, R. (2011). CO_2 migration in saline aquifers. Part 2—Capillary and solubility trapping. *Journal of Fluid Mechanics*, *688*, 321–351.

Maier, C., & Geiger, S. (2013). Multi-rate mass-transfer dual-porosity modelling using the exact analytical solution for spontaneous imbibition (SPE 164926). In *2013 SPE Europec/EAGE annual conference and exhibition*, London, UK, 10–13 June.

March, R., Doster, F., & Geiger, S. (2016). Accurate early-time and late-time modeling of countercurrent spontaneous imbibition. *Water Resources Research*, *52*, 6263–6276. https://doi.org/10.1002/2015WR018456

March, R., Elder, H., Doster, F., & Geiger, S. (2017). Accurate dual-porosity modeling of CO_2 storage in fractured reservoirs (SPE-182646-MS). In *SPE reservoir simulation conference*, Montgomery, USA, 20–22 February.

Moinfar, A., Varavei, A., & Sepehrnoori, K. (2014). Development of an efficient embedded discrete fracture model for 3D compositional reservoir simulation in fractured reservoirs. *SPE Journal*, *19*(2), 289–303.

Moinfar, A., Varavei, A., Sepehrnoori, K., & Johns, R. T. (2013). Development of a coupled dual continuum and discrete fracture model for the simulation of unconventional reservoirs (SPE 163647). In *SPE reservoir simulation symposium*, The Woodlands, USA, 18–20 February.

Nordbotten, J. M., & Celia, M. A. (2012). *Geological storage of CO2: Modeling approaches for large-scale simulation*. Hoboken, NJ: Wiley-Blackwell.

Pacala, S., & Socolow, R. (2004). Stabilization wedges: Solving the climate problem for the next 50 years with current technologies. *Science*, *305*(5686), 968–972.

Pedrera, B., Bertin, H., Bordeaux, U., Hamon, G., & Augustin, A. (2002). Wettability effect on oil relative permeability during a gravity drainage (SPE 77542). In *SPE/DOE thirteenth symposium on improved oil recovery*, Tulsa, USA, 13–17 April.

Pruess, K. (1985). A practical method for modeling fluid and heat flow in fractured porous media. *Society of Petroleum Engineers Journal*, *25*(1), 14–26.

Ramirez, B., Kazemi, H., & Al-Kobaisi, M. (2009). A critical review for proper use of water/oil/gas transfer functions in dual-porosity naturally fractured reservoirs: Part I. *SPE Reservoir Evaluation and Engineering*, *12*(2), 211– 217.

Riaz, A., Hesse, M., Tchelepi, H. A., & Orr, F. M. (2006). Onset of convection in a gravitationally unstable diffusive boundary layer in porous media. *Journal of Fluid Mechanics*, *548*, 87–111.

Ringrose, P. S. (2017). Principles of sustainability and physics as a basis for the low-carbon energy transition. *Petroleum Geoscience*, *23*(3), 287–297. https://doi.org/10.1144/petgeo2016-060

Rossen, W. R., & Kumar, A. (1992). Single- and two-phase flow in natural fractures (SPE 24915). In *67th SPE annual technical conference and exhibition*, Washington DC, USA, 4–7 October.

Schlumberger (2014). *Eclipse technical description*—Eclipse Reservoir Simulation Software Version 2014.1.

Schmid, K. S., & Geiger, S. (2012). Universal scaling of spontaneous imbibition for water-wet systems. *Water Resources Research*, *48*, W03507. https://doi.org/10.1029/2011WR011566

Schmid, K. S., & Geiger, S. (2013). Universal scaling of spontaneous imbibition for arbitrary petrophysical properties: Water-wet and mixed-wet states and Handy's conjecture. *Journal of Petroleum Science and Engineering*, *101*, 44–61.

Schmid, K. S., Geiger, S., & Sorbie, K. S. (2013). Higher order FE–FV method on unstructured grids for transport and two-phase flow with variable viscosity in heterogeneous porous media. *Journal of Computational Physics*, *241*, 416–444.

Shah, S., Møyner, O., Tene, M., Lie, K. A., & Hajibeygi, H. (2016). The multiscale restriction smoothed basis method for fractured porous media (F-MsRSB). *Journal of Computational Physics*, *318*, 36–57.

Spycher, N., Pruess, K., & Ennis-King, J. (2003). CO_2-H_2O mixtures in the geological sequestration of CO_2. I. Assessment and calculation of mutual solubilities from 12 to 100C and up to 600 bar. *Geochimica et Cosmochimica Acta*, *67*(16), 3015–3031.

Suekane, T., Nobuso, T., Hirai, S., & Kiyota, M. (2008). Geological storage of carbon dioxide by residual gas and solubility trapping. *International Journal of Greenhouse Gas Control*, *2*(1), 58–64.

Tecklenburg, J., Neuweiler, I., Carrera, J., & Dentz, M. (2016). Multi-rate mass transfer modeling of two-phase flow in highly heterogeneous fractured and porous media. *Advances in Water Resources*, *91*, 63–77.

Warren, J., & Root, P. (1963). The behavior of naturally fractured reservoirs. *SPE Journal*, *3*(3), 245–255.

Zhou, Q., Oldenburg, C. M., Spangler, L. H., & Birkholzer, J. T. (2017). Approximate solutions for diffusive fracture-matrix transfer: Application to storage of dissolved CO_2 in fractured rocks. *Water Resources Research*, *53*, 1746–1762. https://doi.org/10.1002/2016WR019868

Erratum

Equation (12) was incorrectly given in the originally-published version of this article due to a typesetter error. In addition, the reference to Zhou et al was erroneously written as Zhou et al, 2014, and contained an error in the DOI. It has been fixed as follows to reference to the correct paper: Zhou, Q., Oldenburg, C. M., Spangler, L. H., & Birkholzer, J. T. (2017), Approximate solutions for diffusive fracture-matrix transfer: Application to storage of dissolved CO_2 in fractured rocks, Water Resources Research, 53,1746–1762, doi:10.1002/2016WR019868. All corrections have been made to the online version, which may be considered the authoritative version of record.